

Laser-induced spatiotemporal dynamics of magnetic films

Ka Shen¹ and Gerrit E. W. Bauer^{2,1}

¹*Kavli Institute of NanoScience, Delft University of Technology, Lorentzweg 1, 2628 CJ Delft, The Netherlands*

²*Institute for Materials Research and WPI-AIMR, Tohoku University, Sendai 980-8577, Japan*

(Dated: November 5, 2018)

We present a theory for the coherent magnetization dynamics induced by a focused ultrafast laser beam in magnetic films, taking into account nonthermal (inverse Faraday effect) and thermal (heating) actuation. The dynamic conversion between spin waves and phonons is induced by the magnetoelastic coupling that allows efficient propagation of angular momentum. The anisotropy of the magnetoelastic coupling renders characteristic angle dependences of the magnetization propagation that are strikingly different for thermal and nonthermal actuation.

PACS numbers: 75.80.+q, 75.30.Ds, 75.78.-n, 78.20.Ls

Introduction — Since the discovery of laser-induced ultrafast spin dynamics in Nickel by Beaurepaire *et al.* [1], the spin manipulation in ferromagnetic system by femtosecond laser pulses has attracted much attention since combining the intellectual challenge of new physics with the application potential of ultrafast magnetization reversal [2]. Intense light can cause many effects in magnets, such as the coherent inverse Faraday effect (IFE) as well as the excitation of the coupled electron, magnon and phonon subsystems on various time scales. The associated modulation of the magnetic anisotropy and magnetization modulus allows coherent control of the magnetic order [3, 4]. The transient magnetic field generated by the IFE allows non-thermal ultrafast magnetization control [5, 6] that may be distinguished from heating-induced effects by switching the light polarization. Nevertheless, heating is essential for light-induced magnetization reversal [7]. Toggle switching of the magnetization by heat alone has also been reported [8]. Understanding and controlling the relative magnitude of thermal and non-thermal excitation is therefore an important but unsolved issue.

The optical ultrafast pump-probe technique as shown in Fig. 1 is an established powerful method to study matter. Here we will show that the symmetry of the spatiotemporal magnetization distribution excited by a focused laser beam reveals the relative contributions of thermal and non-thermal excitations. This phenomenon originates from the magnetoelastic coupling (MEC) [9–11], i.e., the coupling between spin waves (magnons) and acoustic lattice waves (phonons).

In the regions of phase space in which the magnon and phonon dispersion come close, the MEC hybridizes magnons and phonons into coherently mixed quasiparticles [“magnon-polarons”(MPs)]. This implies that phonons in magnets can be converted into magnetization and become detectable via magneto-optical [12–14] or electrical [15, 16] techniques. In this Letter, we present a study of the spatial magnetization dynamics in magnetic thin films after focused-laser excitation [17]. We consider here magnetic insulators that are not affected

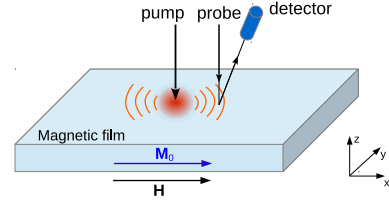


FIG. 1: Pump-probe study of the dynamics of magnetic films by pulsed lasers: An external magnetic field aligns the equilibrium magnetization along the x direction. The pump laser hits the sample at the origin in time and space. The temporal distribution of the out-of-plane (z) component of the magnetization is detected by the Kerr rotation of the linearly polarized probe pulse.

by conduction or photo-excited free carriers. We find that laser-generated phonons efficiently excite magnetization when the diameter of the laser spot is comparable with the wavelength of the MPs. The spatial dynamics of such phonon-induced magnetization shows a different angular symmetry from that of the magnetization generated directly by laser via the IFE. Dedicated experiments suggested here can therefore help understanding the fundamental nature of light-matter interaction in magnets.

Formalism — The basic theory for MPs in special symmetry directions by Kittel [9] and Akhiezer *et al.*[10], extended by Schlömann [11] to arbitrary propagating directions, was developed more than half a century ago. The energy density of the minimal model reads [9]

$$\mathcal{H} = \mathcal{H}_{\text{ex}} + \mathcal{H}_Z + \mathcal{H}_{\text{el}} + \mathcal{H}_{\text{mec}} + \mathcal{H}_{\text{dip}}. \quad (1)$$

We adopt a cubic unit cell and consider the thin film limit in which the magnetization is spatially constant over the film thickness. This assumption holds for films up to $100 \mu\text{m}$ [17], which for wide-gap insulators is still less than the penetration depth of the light and allows us to use a two-dimensional model. With external magnetic field \mathbf{H} and equilibrium magnetization vector $\mathbf{M}_0 \parallel \mathbf{x}$ ($|\mathbf{M}_0| = M_0$ saturation magnetization) $\mathcal{H}_{\text{ex}} = A[(\nabla m_y)^2 + (\nabla m_z)^2]$ and $\mathcal{H}_Z = -\mu_0 H M_0 +$

$(\mu_0 H M_0/2)(m_y^2 + m_z^2)$ represent the (linearized) exchange and Zeeman energies, respectively, where m_y and m_z are the transverse magnetization components of $\mathbf{m} = \mathbf{M}/M_0$. \mathcal{H}_{el} is the lattice energy with both kinetic and elastic contributions $\mathcal{H}_{\text{el}} = (1/2)\rho\dot{\mathbf{R}} \cdot \dot{\mathbf{R}} + (1/2)\lambda(\sum_i S_{ii})^2 + \mu\sum_{ij} S_{ij}^2$ with strain tensor $S_{ij} = (\partial_i R_j + \partial_j R_i)/2$ and \mathbf{R} representing the lattice displacement with respect to equilibrium, ρ the mass density, and λ and μ elastic constants. The MEC in Eq. (1) reads $\mathcal{H}_{\text{mec}} = \sum_{i,j \in \{y,z\}} (b + a\delta_{ij})S_{ij}m_i m_j + 2b\sum_{i \in \{y,z\}} S_{ix}m_i$, where a and b are magnetoelastic coupling coefficients. By adopting the short-wave length limit of the magnetostatic dipolar interaction $\mathcal{H}_{\text{dip}} \approx (\mu_0 M_0^2/2)m_y^2 \sin^2 \theta$, we disregard the Damon-Eshbach surface modes [18] and simplify the dispersion of the volume modes, which is allowed for small laser spot sizes with response being dominated by high-momentum wave vectors [19].

By introducing the forces and torques \mathbf{F} acting on the displacement vector $\Phi = (m_y, m_z, R_x, R_y, R_z)^T$, one can write out the linearized equations of motion as shown in the Supplemental Material [20]. Here, the lattice displacement is rewritten in the form of longitudinal (R_x), in-plane transverse (R_y) and out-of-plane transverse (R_z) modes. Strictly speaking, the damping of phonons and magnon are not necessarily independent, since magnetization is affected by phonon attenuation via the MEC [27]. We treat Gilbert damping constant α and phonon relaxation time τ_p as independent parameters since Gilbert damping can also be caused by magnetic disorder, surface roughness or defects [28]. We define the anisotropic spin wave frequency $\Omega_0 = \gamma\mu_0\sqrt{H(H + M_0 \sin^2 \theta)}$ and the MEC frequency parameter $\Delta(k) = \sqrt{\gamma b^2 k^2 / (4M_0 \rho \Omega_0)}$ with θ being the angle between magnetic field and in-plane wave vector \mathbf{k} .

The spatiotemporal dynamics of $\Phi(\mathbf{r}, t)$ reads

$$\Phi_i(\mathbf{r}, t) = \int d\mathbf{r}' dt' G_{ij}(\mathbf{r} - \mathbf{r}', t - t') F_j(\mathbf{r}', t'), \quad (2)$$

where G_{ij} are the components of the Green function matrix (propagator) associated with the magnetoelastic equations of motion specified in the Supplement [20]. A femtosecond laser pulse generates forces via the inverse Faraday effect [2, 17, 29] and heating [14, 30–32] that are instantaneous on the scale of the lattice and magnetization dynamics. The relative importance of these two mechanisms depends on the material and light and is still a matter of controversy. Here we find that spot excitation of thin magnetic films is an appropriate method to separate the two, since they lead to conspicuous differences in the time and position dependent response.

We consider circularly polarized light along z that by the IFE generates an effective magnetic field along the same direction. For a femtosecond Gaussian pulse with spot size W , the generated magnetic field has a spatial distribution $\mathbf{H}_{\text{IFE}}(\mathbf{r}, t) = \hat{z}H_{\text{IFE}}f(t)\exp(-r^2/W^2)$ where

temporal shape $f(t) \approx \tau_l \delta(t)$ with pulse duration τ_l ; the amplitude $H_{\text{IFE}} = \beta I_{\text{in}} \sigma$ is proportional to laser intensity (I_{in}) and IFE coefficient (β), respectively. The latter is related to the Verdet constant (V) as $\beta = V\lambda_0/(2\pi c_0)$, where λ_0 and c_0 are wavelength and velocity of the light [33]. $\sigma = 1(-1)$ for left(right)-handed polarization. The torque $F_{m_y}(\mathbf{r}, t) = \gamma\tau_l\mu_0 H_{\text{IFE}}\delta(t)\exp(-r^2/W^2)$. On the other hand, the light pulse generates a sudden increase of the local lattice temperature $\delta T(\mathbf{r}, t) = [\Gamma I_{\text{in}}\tau_l/(\rho C_v)]\Theta(t)\exp(-r^2/W^2)$, where Γ is the light-absorption coefficient. By choosing the Heaviside step function $\Theta(t)$ we assume that the lattice locally equilibrates much faster than the response time of the coherent magnetization (a few picoseconds [34]), while the subsequent cooling of the lattice by diffusion is slow. The resulting in-plane thermoelastic stress $F_{R_x} = \eta(3\lambda + 2\mu)\partial_r T$ generates longitudinal (pressure) waves [31, 35], where η is the thermoelastic expansion coefficient. The local thermal expansion also generates a “bulge” shear stress [36] at a free surface, i.e., an out-of-plane displacement R_z . $F_{R_z} = \zeta\eta\nabla^2 T$, where ζ is a parameter proportional to the film thickness and controlled by the substrate and an eventual cap layer, leads to displacement proportional to local temperature gradient (see numerical results below). In the Supplemental Material [20], we specify the material parameters for yttrium iron garnet (YIG) adopted in our calculations.

One-dimensional dynamics — We start with a spin wave propagating along the external magnetic field, i.e., $\theta = 0$, which by symmetry couples only with the transverse phonons. The IFE generates the torque $F_{m_y}(x, t) = m_0\delta(t)\exp(-x^2/W^2)$ with $m_0 = \gamma\tau_l\mu_0 H_{\text{IFE}}$. This can be realized by a line-shaped excitation spot [17].

The calculated magnetization profiles at $\Omega_0 t = 50$ and 75 without and with MEC are plotted in Fig. 2(a) and (b) separately for $\alpha = 10^{-4}$. Without MEC the magnetization is localized at the exposure spot and broadens only very weakly with time while the MEC strongly enhances the broadening of primary magnetization packet, with a wavefront propagating with the sound velocity c_t . This phenomenon illustrates that the lattice plays an essential role for spin transport in magnetic films.

Fig. 2(c) illustrates the sound-assisted propagation for Gilbert damping $\alpha = 0.1$. Instead of the expanding wave front in Fig. 2(b), we now find two packets escaping the excitation region into opposite directions. The packets have a much longer lifetime than the coherently generated IFE magnetization, hence dominate at long time scales. This behavior is recovered by the asymptotic expression obtained when $\alpha \gg \tilde{\Delta}(\tilde{k}_c)$ at the magnon-phonon dispersion crossing wave vector ($\tilde{k}_c = 1/\tilde{c}_t$),

$$m_z(\tilde{x}, \tilde{t}) \simeq m_0 e^{-\alpha\tilde{t} - \tilde{x}^2} \sin(\tilde{t}) + (2\alpha)^{-1} m_0 e^{-\tilde{t}/\tilde{\tau}_p} \tilde{\Delta}^2(\tilde{k}_c) \times \begin{cases} 2\tilde{\alpha}\tilde{c}_t^2 [\Lambda_1(\tilde{c}_t\tilde{t} - \tilde{x}) + \Lambda_1(\tilde{c}_t\tilde{t} + \tilde{x})], & \tilde{c}_t \ll 1, \\ \tilde{c}_t^{-1}\sqrt{\pi} [\Lambda_2(\tilde{c}_t\tilde{t} - \tilde{x}) + \Lambda_2(\tilde{c}_t\tilde{t} + \tilde{x})], & \tilde{c}_t \geq 1, \end{cases} \quad (3)$$

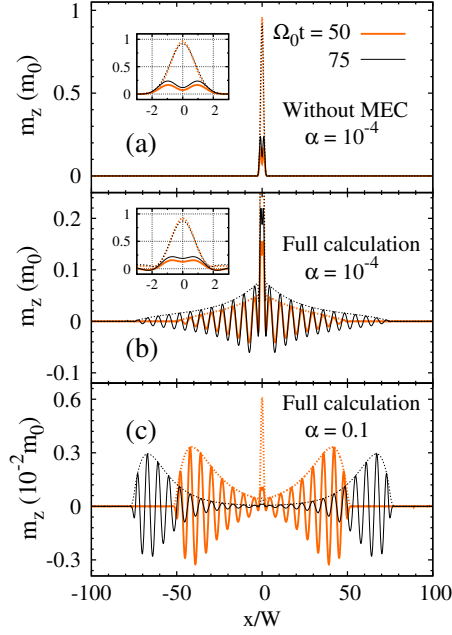


FIG. 2: (Color online) One-dimensional model for the dynamics of the out-of-plane magnetization component m_z induced by the inverse Faraday effect: (a) At times $\Omega_0 t = 50$ and 75 for a Gaussian laser intensity spot in the absence of MEC with Gilbert damping $\alpha = 10^{-4}$. The dashed envelopes are the modulus ($|\mathbf{m} - \hat{x}|$). (b) with $\alpha = 10^{-4}$ and (c) with $\alpha = 0.1$ are computed for MEC parameter $\hat{\Delta}(\tilde{k}_c) = 0.02$. Common are the exchange parameter $\hat{D} = 0.02$, sound velocity $\tilde{c}_t = 1$, and sound attenuation rate $\tilde{\tau}_p^{-1} = 10^{-3}$. Note the change of scale between (b) and (c). The insets provide an expanded view of the laser spot.

where $\Lambda_1(\xi) = (1/\sqrt{\pi}) \int_0^\infty d\tilde{k} \tilde{k}^2 \sin(\tilde{k}\xi) \exp(-\tilde{k}^2/4)$ and $\Lambda_2(\xi) = \exp[-(\xi^2\alpha^2 + 1)/(2\tilde{c}_t^2)] \sin(\xi/\tilde{c}_t)$ and W and Ω_0 have been by rendered dimensionless as explained in the Supplemental Material [20]. The (purely magnetic) first term on the right-hand side represent the exponential decay of the initially excited wave packet, while the second term is a propagating MP mode. The latter decays with the phonon damping rate, hence may have a very long mean free path for materials with high acoustic quality like YIG (assuming that doping affects the magnetization without increasing sound attenuation).

When the laser spot size is large relative to the MP wave length, i.e., $\tilde{c}_t \ll 1$, according to Eq. (3) the ratio between MP amplitude and IFE strength scales as $\tilde{c}_t^2 \hat{\Delta}^2(\tilde{k}_c)$, i.e., increases with sound velocity and decreases with spot size. In the other limit, $\tilde{c}_t \gg 1$, the amplitude of the long-lived signal is inversely proportional to \tilde{c}_t , therefore decreases with increasing \tilde{c}_t . We therefore estimate this ratio to be maximal $e^{-1/4} \sqrt{\pi} \hat{\Delta}^2(\tilde{k}_c)/(2\alpha)$ when the laser spot size matches the MP wave length. The peak amplitude of MPs in Fig. 2(c) is around 3×10^{-3} , in good agreement with $e^{-1/4} \sqrt{\pi} \hat{\Delta}^2(\tilde{k}_c)/(2\alpha) \approx$

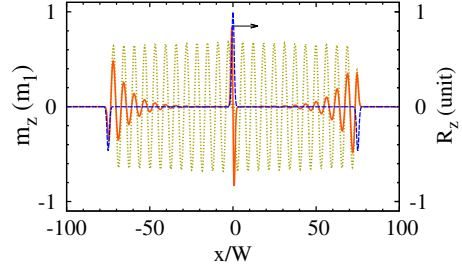


FIG. 3: (Color online) Out-of-plane magnetization dynamics m_z with Gilbert damping $\alpha = 10^{-4}$ (dotted curve) and 0.1 (solid curve) induced by the spot heating by a laser pulse. The blue dashed curve shows the displacement profile (R_z). Other parameters are those in Fig. 2.

2.7×10^{-3} .

Thermal actuation is caused by the shear force generated by the laser heating profile $F_{R_z}(x, t) = (\zeta\eta c_t^2 \Gamma I_{in} \tau_l / C_v) \Theta(t) \partial_x^2 \exp(-x^2/W^2)$, since the pressure wave is decoupled from the spin wave at $\theta = 0$. The asymptotic expression for $\alpha \gg \hat{\Delta}(\tilde{k}_c)$ becomes

$$m_z(x, t) = m_1 \times \begin{cases} \tilde{c}_t \{ \Lambda_3(\tilde{x}) - (1/2)e^{-\tilde{t}/\tilde{\tau}_p} \\ \times [\Lambda_3(\tilde{c}_t \tilde{t} + \tilde{x}) - \Lambda_3(\tilde{c}_t \tilde{t} - \tilde{x})] \} & , \quad \tilde{c}_t \ll 1, \\ \tilde{c}_t (1 - e^{-\alpha t} \cos t) \Lambda_3(\tilde{x}) + \tilde{c}_t^{-1} (\sqrt{\pi}/4) \\ \times e^{-\tilde{t}/\tilde{\tau}_p} [\Lambda_4(\tilde{c}_t \tilde{t} + \tilde{x}) - \Lambda_4(\tilde{c}_t \tilde{t} - \tilde{x})] & , \quad \tilde{c}_t \geq 1, \end{cases} \quad (4)$$

where $\Lambda_3(\xi) = \xi \exp(-\xi^2)$ and $\Lambda_4(\xi) = \exp[-(\xi^2\alpha^2 + 1)/(2\tilde{c}_t^2)] \cos(\xi/\tilde{c}_t)$. For YIG, the parameter $m_1 = \gamma b \zeta \eta \Gamma I_{in} \tau_l / (2M_0 \rho c_t C_v) \sim 10^3 \zeta \delta T \text{ m}^{-1} \text{ K}^{-1}$. Compared to Eq. (3), the heat-induced magnetization has (i) odd parity in real space, i.e., $m_z(-x, t) = -m_z(x, t)$, (ii) a long-lived localized signal near the excitation spot, and (iii) maximum amplitude of propagation at $\tilde{c}_t \simeq 1$, cf. Fig. 3. We also plot the amplitude of the thermally generated phonon wave front that is trailed by the magnetization.

Two Dimensions — In the following, magnetization is oriented along \hat{x} by an external in-plane magnetic field $\mu_0 H = 50 \text{ mT}$ corresponding to $\gamma \mu_0 H / (2\pi) \simeq 1.4 \text{ GHz}$. The spot size $W = 1 \mu\text{m}$ and the dimensionless velocities are $\tilde{c}_t \approx 0.43$ and $\tilde{c}_l \approx 0.82$. Fig. 4 summarizes our main results for the IFE and heat induced dynamics in terms of the out-of-plane magnetization component m_z . We plot a snapshot at $t = 5 \text{ ns}$ in the x - y (film) plane from the calculation with low ($\alpha = 10^{-4}$) and enhanced ($\alpha = 0.1$) magnetic damping in (a) and (b), respectively. Fig. 4(a, left) displays IFE actuated outgoing rays that broaden with distance from the excitation spot. This feature is insensitive to MEC strength and can be understood by the angular dependent group velocities of magnetostatic spin wave dispersion around

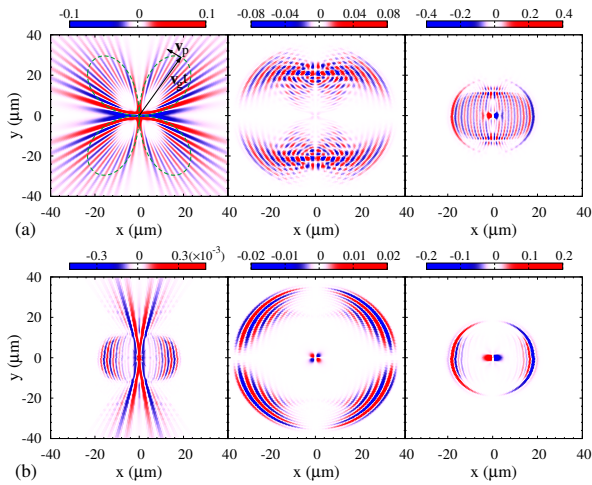


FIG. 4: (Color online) Two dimensional profile of out-of-plane magnetization, m_z , at $t = 5$ ns due to (left) IFE field F_{m_y} , (middle) pressure stress F_{R_l} and (right) shear stress F_{R_z} . We normalize the result by m_0 for (left), $m_2 = \gamma b \eta \Gamma I_{in} \tau_l (3\lambda + 2\mu) / (2M_0 \rho^2 C_v c_t^2 \Omega_0)$ for (middle) and m_1 for (right). The Gilbert damping coefficient $\alpha = 10^{-4}$ and 0.1 for (a) and (b), respectively. The dashed (olive) curve in (a, left) illustrates the angular-dependent spin wave group velocity.

the average modulus of the wave vectors k_0 . As discussed in the Supplemental Material [20], the group velocity $\mathbf{v}_g \simeq \hat{\theta} [\gamma \mu_0 M_0 / (2k_0)] \sin 2\theta \sqrt{H / (H + M_0 \sin^2 \theta)}$ generates an expansion of the initial wave packet as shown by the dashed (olive) curve, while the star-like interference fringes are governed by the phase velocity. At larger magnetic damping, cf. Fig. 4(b, left), the star-like features in the \hat{x} direction are suppressed in favor of MP propagation with transverse sound velocity c_t . Dotted feature around $c_l t$ are caused by interference of the longitudinal MP and the damped residue of the initial magnetization wave packet with $\theta \simeq 0$, which has relative longer lifetime. Note the mirror symmetry with respect to the y axis, $m_z(x, y) = m_z(-x, y)$.

The quadrupolar features in Figs. 4(middle) with nodes along the x and y axes and $\sin 2\theta$ symmetry are induced by the pressure F_{R_l} caused by a heat pulse. The radii of the circular wave fronts correspond to the longitudinal sound velocity. Figs. 4(right) illustrate that a shear stress induces MPs that spread with transverse sound velocity c_t , which are thereby clearly distinguishable from the pressure induced signals: F_{R_z} generates dipolar symmetric features with nodes at the y axis, which follows from the $\cos \theta$ symmetry of the MEC coupling. Clearly, both heat-induced signals are antisymmetric with respect to reflection at the y axis, $m_z(x, y) = -m_z(-x, y)$, which allows discrimination from the IFE response. Moreover, we identify a non-propagating signal in the vicinity of the excitation spot [see the center of Figs. 4(b, middle) and (b, right)], a “smoking gun” for thermally excited

dynamics.

It is not easy to predict the absolute and relative magnitude of the two mechanisms for a given light intensity from first principles due to uncertainties in the strongly non-equilibrium processes after an intense fs light pulse. Microscopic theories address the ultra-fast physics of angular momentum and energy transfer from the light to the magnetic order [37, 38] and the lattice [34] and should ideally be employed to fix the initial conditions for our calculations. But also the long-time response depends on several temperature and frequency dependent materials parameters that govern the IFE, light absorption etc. Satoh *et al.* [17] find a Faraday rotation of the probe pulse of the order of milli-rad for $110 \mu\text{m}$ thick bismuth-doped iron garnet, which corresponds to a light-induced torque of $m_0 \sim 0.004$ for a Verdet constant of $10^4 \text{ rad m}^{-1} \text{ T}^{-1}$ [20]. With thermal expansion coefficient $\eta \sim 10^{-5} / \text{K}$ [39], the thermal torque $m_2 \sim 4 \times 10^{-3} \delta T / \text{K}$, which can be larger than m_0 for pulsed laser-induced heating [40]. Similar values may be anticipated for m_1 when effective thicknesses $\zeta \sim \mu\text{m}$. We should also not forget that the fast light-induced demagnetization [1] should affect the response directly under the excitation spot, but its diffusion should be slower than the ballistic response computed here.

Conclusion and Discussion — We modeled the spatiotemporal laser-induced magnetization dynamics in magnetic thin films, concluding that magnetoelastic coupling is essential for spin angular momentum transport because the phonon group velocity is much larger than that of the magnons. An experimental study of the symmetry of time-resolved magnetization wave fronts radiating from the excitation spot allows discriminating different laser excitation mechanisms, thereby helping to answer the long-standing question on the physical origin of ultra-fast magnetization dynamics, i.e. whether it is caused by coherent light-induced magnetic fields or sudden heating of the lattice. Moreover, we clarified the optimal size of the excitation laser spot to be the MP wavelength; for YIG at an applied field of 50 mT it is $\sim 1 \mu\text{m}$.

The essential role of the MEC coupling might have larger ramifications. For example, a number of recent experiments on the spin Seebeck effect on YIG came to the conclusion that the thermal spin pumping is not caused by terahertz magnons at energies around $k_B T$, but by spin waves in a low energy band close to the gap [41–43]. Spin information was found to propagate in YIG diffusely over large distances [44, 45]. From the present results we venture that strongly coupled magnon-polarons could be the carriers of thermal spin currents.

This work is supported by the DFG Priority Program 1538 SpinCat, the FOM foundation, the E-IMR and ICC-IMR, and the JSPS (Grant Nos. 25247056, 25220910, 26103006). We acknowledge discussions with Benedetta Flebus and Rembert Duine.

Note added in proof: Ogawa *et al.* report generation of laser-generated magnon polarons that drive magnetic bubble domains [46].

-
- [1] E. Beaurepaire, J.-C. Merle, A. Daunois, and J.-Y. Bigot, *Phys. Rev. Lett.* **76**, 4250 (1996).
- [2] A. Kirilyuk, A. V. Kimel, and T. Rasing, *Rev. Mod. Phys.* **82**, 2731 (2010).
- [3] G. Ju, A. V. Nurmikko, R. F. C. Farrow, R. F. Marks, M. J. Carey, and B. A. Gurney, *Phys. Rev. Lett.* **82**, 3705 (1999).
- [4] M. van Kampen, C. Jozsa, J. T. Kohlhepp, P. LeClair, L. Lagae, W. J. M. de Jonge, and B. Koopmans, *Phys. Rev. Lett.* **88**, 227201 (2002).
- [5] A. V. Kimel, A. Kirilyuk, P. A. Usachev, R. V. Pisarev, A. M. Balbashov, and T. Rasing, *Nature* **435**, 655 (2005).
- [6] F. Hansteen, A. Kimel, A. Kirilyuk, and T. Rasing, *Phys. Rev. Lett.* **95**, 047402 (2005).
- [7] K. Vahaplar, A. M. Kalashnikova, A. V. Kimel, D. Hinzke, U. Nowak, R. Chantrell, A. Tsukamoto, A. Itoh, A. Kirilyuk, and T. Rasing, *Phys. Rev. Lett.* **103**, 117201 (2009).
- [8] J. Barker, U. Atxitia, T. A. Ostler, O. Hovorka, O. Chubykalo-Fesenko, and R. W. Chantrell, *Scientific Report* **3**, 3262 (2013).
- [9] C. Kittel, *Phys. Rev.* **110**, 836 (1958).
- [10] A. I. Akhiezer, V. G. Bar'yakhtar, and S. V. Peletminskii, *Zh. Eksp. Teor. Fiz* **35**, 228 (1958).
- [11] E. Schlömann, *J. Appl. Phys.* **31**, 1647 (1960).
- [12] A. V. Scherbakov, A. S. Salasyuk, A. V. Akimov, X. Liu, M. Bombeck, C. Brüggemann, D. R. Yakovlev, V. F. Sapega, J. K. Furdyna, and M. Bayer, *Phys. Rev. Lett.* **105**, 117204 (2010).
- [13] J.-W. Kim, M. Vomer, and J.-Y. Bigot, *Phys. Rev. Lett.* **109**, 166601 (2012).
- [14] J. V. Jäger, A. V. Scherbakov, B. A. Glavin, A. S. Salasyuk, R. P. Campion, A. W. Rushforth, D. R. Yakovlev, A. V. Akimov, and M. Bayer, *arXiv:1505.01729*.
- [15] K. Uchida, H. Adachi, T. An, T. Ota, M. Toda, B. Hillebrands, S. Maekawa, and E. Saitoh, *Nature Mater.* **10**, 737 (2011).
- [16] M. Weiler, H. Huebl, F. S. Goerg, F. D. Czeschka, R. Gross, and S. T. B. Goennenwein, *Phys. Rev. Lett.* **108**, 176601 (2012).
- [17] T. Satoh, Y. Terui, R. Moriya, B. A. Ivanov, K. Ando, E. Saitoh, T. Shimura, and K. Kuroda, *Nature Photonics* **6**, 662 (2012).
- [18] R. W. Damon and J. R. Eshbach, *J. Phys. Chem. Solids* **19**, 308 (1961).
- [19] A. A. Serga, P. Clausen, A. V. Chumak, and B. Hillebrands, *Annual Report 2012*, <http://www.physik.uni-kl.de/hillebrands/publications/annual-reports/annual-report-2012>.
- [20] See Supplemental Material contains technical discussions with reference to [21–26].
- [21] S. A. Manuilov, S. I. Khartsev, and A. M. Grishin, *J. Appl. Phys.* **106**, 123917 (2009).
- [22] A. G. Gurevich and G. A. Melkov, *Magnetization Oscillations and Waves* (CRC Press, Boca Raton, 1996).
- [23] A. A. Serga, A. V. Chumak, and B. Hillebrands, *J. Phys. D: Appl. Phys.* **43**, 264002 (2010).
- [24] M. A. Gilleo and S. Geller, *Phys. Rev.* **110**, 73 (1958).
- [25] M. F. Lewis and E. Patterson, *J. Appl. Phys.* **39**, 1932 (1968).
- [26] J. G. Bai, G.-Q. Lu, and T. Lin, *Sensors and Actuators A: Physical* **109**, 9 (2003).
- [27] C. Vittoria, S. D. Yoon, and A. Widom, *Phys. Rev. B* **81**, 014412 (2010).
- [28] G. G. Siu, C. M. Lee, and Y. Liu, *Phys. Rev. B* **64**, 094421 (2001).
- [29] A. H. M. Reid, A. V. Kimel, A. Kirilyuk, J. F. Gregg, and T. Rasing, *Phys. Rev. B* **81**, 104404 (2010).
- [30] O. B. Wright and K. Kawashima, *Phys. Rev. Lett.* **69**, 1668 (1992).
- [31] C. Rossignol, J. M. Rampnoux, M. Perton, B. Audoin, and S. Dilhaire, *Phys. Rev. Lett.* **94**, 166106 (2005).
- [32] H. Park, X. Wang, S. Nie, R. Clinite, and J. Cao, *Phys. Rev. B* **72**, 100301 (2005).
- [33] P. S. Pershan, J. P. van der Ziel, and L. D. Malmstrom, *Phys. Rev.* **143**, 574 (1966).
- [34] E. S. Zijlstra, A. Kalitsov, T. Zier, and M. E. Garcia, *Phys. Rev. X* **3**, 011005 (2013).
- [35] S. J. Davies, C. Edwards, G. S. Taylor, and S. B. Palmer, *J. Phys. D: Appl. Phys.* **26**, 329 (1993).
- [36] R. J. Dewhurst, D. A. Hutchins, S. B. Palmer, and C. B. Scruby, *J. Appl. Phys.* **53**, (1982).
- [37] G. Lefkidis, G. P. Zhang, and W. Hübner, *Phys. Rev. Lett.* **103**, 217401 (2009).
- [38] U. Atxitia, O. Chubykalo-Fesenko, R. W. Chantrell, U. Nowak, and A. Rebei, *Phys. Rev. Lett.* **102**, 057203 (2009).
- [39] T. Boudiar, B. Payet-Gervy, M.-F. Blanc-Mignon, J.-J. Rousseau, M. L. Berre, and H. Joisten, *J. Magn. Magn. Mater.* **284**, 77 (2004).
- [40] G.-M. Choi, C.-H. Moon, B.-C. Min, K.-J. Lee, and D. G. Cahill, *Nature Phys.* **11**, 576 (2015).
- [41] T. Kikkawa, K.-i. Uchida, S. Daimon, Z. Qiu, Y. Shiomi, and E. Saitoh, *Phys. Rev. B* **92**, 064413 (2015).
- [42] H. Jin, S. R. Boona, Z. Yang, R. C. Myers, and J. P. Heremans, *Phys. Rev. B* **92**, 054436 (2015).
- [43] E. Guo, A. Kehlberger, J. Cramer, G. Jakob, and M. Kläui, *arXiv:1506.06037*.
- [44] L. J. Cornelissen, J. Liu, R. A. Duine, J. Ben Youssef, and B. J. van Wees, *Nature Phys.* (in press).
- [45] B. L. Giles, Z. Yang, J. Jamison, and R. C. Myers, *arXiv:1504.02808*.
- [46] N. Ogawa, W. Koshibae, A. J. Beekman, N. Nagaosa, M. Kubota, M. Kawasaki, and Y. Tokura, *PNAS* **112**, 8977 (2015).

Supplementary material to “Laser-induced spatiotemporal dynamics of magnetic films”

Ka Shen¹ and Gerrit E. W. Bauer^{2,1}

¹*Kavli Institute of NanoScience, Delft University of Technology, Lorentzweg 1, 2628 CJ Delft, The Netherlands*

²*Institute for Materials Research and WPI-AIMR, Tohoku University, Sendai 980-8577, Japan*

This supplement includes the linearized equations of motion in Fourier space with choice of parameters, as well as analytical expression for the IFE-induced dynamical response to line and point sources and estimation on the magnitude of IFE.

1. LINEARIZED EQUATIONS OF MOTION IN FOURIER SPACE

After introducing the forces and torques \mathbf{F} acting on the displacement vector $\Phi = (m_y, m_z, R_l, R_t, R_z)^T$, the linearized equations of motion in Fourier space read [1]

$$(\omega^2 - 2i\omega\tau_p^{-1} - c_t^2 k^2)\rho R_t = ibk \cos 2\theta m_y - F_{R_t}, \quad (\text{S1})$$

$$(\omega^2 - 2i\omega\tau_p^{-1} - c_t^2 k^2)\rho R_z = ibk \cos \theta m_z - F_{R_z}, \quad (\text{S2})$$

$$(\omega^2 - 2i\omega\tau_p^{-1} - c_l^2 k^2)\rho R_l = ibk \sin 2\theta m_y - F_{R_l}, \quad (\text{S3})$$

$$i\omega m_y + (\gamma H_k + i\alpha\omega)m_z = i\Delta_1 \cos \theta R_z + F_{m_y}, \quad (\text{S4})$$

$$i\omega m_z - (\gamma H'_k + i\alpha\omega)m_y = -i\Delta_1 (\cos 2\theta R_t + \sin 2\theta R_l) + F_{m_z}, \quad (\text{S5})$$

where $\Delta_1 = \gamma bk/M_0$, $H'_k = H_k + \mu_0 M_0 \sin^2 \theta$ with $H_k = \mu_0 H + \gamma^{-1}(2A/M_0)k^2$, and θ is the angle between magnetic field and in-plane wave vector \mathbf{k} . α and τ_p are the Gilbert damping constant and phonon relaxation time [2].

We adopt the material parameters of yttrium iron garnet (YIG). Specifically, the dipolar field and gyromagnetic ratio are $\mu_0 M_0 = 175$ mT and $\gamma/2\pi = 2.8 \times 10^{10}$ Hz/T, respectively [3]. The MEC constant $b = 6.96 \times 10^5$ J/m³ [4], the exchange parameter $2A/M_0 = 9.2 \times 10^{-6}$ m²/s [5], and the mass density $\rho = 5170$ kg/m³ [6]. The transverse and longitudinal sound velocities are $c_t = 3.8 \times 10^3$ m/s and $c_l = 7.2 \times 10^3$ m/s [4]. The phonon relaxation rate in YIG is of the order of $1 \mu\text{s}^{-1}$ [7]. In high quality films, the Gilbert damping coefficient is typically around 10^{-4} [3]. For comparison, we also show results for $\alpha = 0.1$, which is close to the upper limit for Bi-doped YIG [8].

2. ANALYTICAL EXPRESSION FOR IFE-INDUCED ONE-DIMENSIONAL DYNAMICS

The time evolution of the out-of-plane magnetization Eq. (2) of the main text can be simplified to

$$m_z(\tilde{x}, \tilde{t}) = \frac{m_0}{\sqrt{\pi}} \sum_{\pm} \int_0^{\infty} d\tilde{k} e^{-\tilde{k}^2/4} \text{Im} \left(\frac{\tilde{\omega}_{\mp} - \tilde{\Omega}_0}{\tilde{\omega}_{\mp} - \tilde{\omega}_{\pm}} e^{i\tilde{\omega}_{\pm}\tilde{t}} \right) \cos \tilde{k}\tilde{x},$$

where $\omega_{\pm} = \left[\tilde{\Omega}_0 + \tilde{\Omega}_p \pm \sqrt{(\tilde{\Omega}_0 - \tilde{\Omega}_p)^2 + 8\tilde{\Delta}^2} \right] / 2$. Here $\tilde{\Omega}_0 = (1 + i\alpha)(1 + \tilde{D}\tilde{k}^2)$, $\tilde{\Omega}_p = \tilde{c}_t\tilde{k} + i\tilde{\tau}_p^{-1}$, $\tilde{k} = kW$, $\tilde{x} = x/W$, $\tilde{\tau}_p = \Omega_0\tau_p$, $\tilde{\Delta} = \Delta/\Omega_0$, $\tilde{c}_t = c_t/(W\Omega_0)$, $\tilde{t} = \Omega_0 t$, and $\tilde{D} = 2A/(M_0\Omega_0 W^2)$ are all dimensionless.

3. ANALYSIS OF STAR-LIKE FEATURE DUE TO IFE FROM POINT SOURCES

The IFE-amplitude induced by an axially symmetric light pulse as plotted in Fig. 4(a,left) displays suprisingly complex interference patterns. These features can be explained in terms of the angular-dependent group velocity at constant $k_0 = \langle |\mathbf{k}| \rangle$ [yellow circle in the (volume) spin wave dispersion shown in Fig. S1(a)]. The thin (black) arrows indicate the group velocities $\mathbf{v}_g \equiv \nabla_{\mathbf{k}}\omega_{\mathbf{k}}|_{k_0, \theta} \simeq \hat{\theta}[\gamma\mu_0 M_0/(2k_0)] \sin(2\theta) \sqrt{H/(H + M_0 \sin^2 \theta)}$, where we used the simplified dispersion $\omega_{\mathbf{k}} \simeq \gamma\mu_0 \sqrt{H(H + M_0 \sin^2 \theta)}$ that is accurate for not too small $k_0 \gtrsim 1/W$. In this approximation

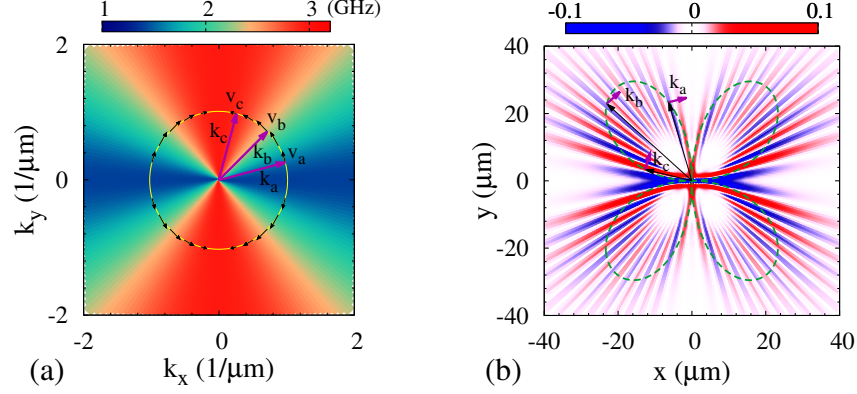


FIG. S1: (Color online) (a) Approximate (bulk) spin wave spectrum $\omega_{\mathbf{k}} = \gamma\mu_0\sqrt{H(H + M_0 \sin^2 \theta)}$ in \mathbf{k} -space. The thin (black) arrows show angular dependence of the group velocities $\mathbf{v}_g = \nabla_{\mathbf{k}}\omega_{\mathbf{k}}$ at the average modulus $k_0 = \langle |\mathbf{k}| \rangle$. Those for three typical wave vectors $\mathbf{k}_{a,b,c}$ represented by thick (purple) arrows are labeled by $\mathbf{v}_{a,b,c}$. (b) Replotting of Fig.4(a,left), IFE-induced magnetization profile in real space at 5 ns, with three thin (black) [thick (purple)] arrows representing $t\mathbf{v}_{a,b,c}$ [$\mathbf{k}_{a,b,c}$].

$\mathbf{v}_g \cdot \mathbf{k} = 0$, i.e., the group velocity is purely transverse. The thick (purple) arrows Fig. S1(a) represent three typical wave vectors $\mathbf{k}_{a,b,c}$, whose corresponding group velocities are labeled by $\mathbf{v}_{a,b,c}$ respectively. In Fig. S1(b), we replot the IFE-induced magnetization profile in real space with dashed (olive) curve representing $t|\mathbf{v}_g|$ and the vectors $\mathbf{k}_{a,b,c}$ and $t\mathbf{v}_{a,b,c}$ as thick (purple) and thin (black) arrows for $t = 5$ ns. We can understand this pattern in terms of the time dependence of a linear superposition of wave packets arranged around the origin: Each wave packet centered around a certain \mathbf{k}_0 is modulated in the direction \hat{k}_0 with wavelength $1/k_0$. The whole package moves rigidly in the transverse direction with group velocity \mathbf{v}_g that is finite by the dipolar interaction. The initial wave packet at the origin thereby blows up like $|\mathbf{v}_g|$. The interference pattern initially normal to \mathbf{k}_0 is in real space shifted and combines with the patterns generated by other wave packets on the ring to form complex features that in the snapshot plotted in the figures look like a star. Moreover, the lifetime of spin waves is determined by $1/(\alpha\omega_{\mathbf{k}})$, leading to $\tau_{\mathbf{k}_a} > \tau_{\mathbf{k}_b} > \tau_{\mathbf{k}_c}$. This explains that even for large dampings a radial pattern is still visible near the y -axis while that along the x -axis has disappeared [see Fig. 4(b,left)].

Analytically, the out-of-plane magnetization at $\mathbf{r} = (r \cos \varphi, r \sin \varphi)$ with respect to the center of initial spot can be expressed as

$$m_z(r, \varphi, t) \propto \int_0^{2\pi} d\theta e^{-\alpha t \gamma \mu_0 \sqrt{H(H + M_0 \sin^2 \theta)}} \int_0^\infty d\tilde{k} \tilde{k} e^{-\tilde{k}^2/4} \cos\left(\tilde{k} \tilde{r} \cos(\theta - \varphi) - t \gamma \mu_0 \sqrt{H(H + M_0 \sin^2 \theta)}\right). \quad (\text{S6})$$

Far from the excitation spot, i.e., $\tilde{r} \gg 1$, the \tilde{k} -integral is dominated by the spin waves satisfying $\cos(\theta - \varphi) \sim 0$ or $\theta \sim \varphi \pm \pi/2$. Taylor-expanding in the phase factor of the cosine leads to

$$\begin{aligned} m_z(r, \varphi, t) &\sim e^{-\alpha t \gamma \mu_0 \sqrt{H(H + M_0 \cos^2 \varphi)}} \int_0^\infty d\tilde{k} \tilde{k} e^{-\tilde{k}^2/4} \int_{-\delta\theta}^{\delta\theta} d\theta' \cos\left(\tilde{k}(\tilde{r} - t|v_g|)\theta' - t \gamma \mu_0 \sqrt{H(H + M_0 \cos^2 \varphi)}\right) \\ &\sim 2 \cos\left(t \gamma \mu_0 \sqrt{H(H + M_0 \cos^2 \varphi)}\right) e^{-\alpha t \gamma \mu_0 \sqrt{H(H + M_0 \cos^2 \varphi)}} \int_0^\infty d\tilde{k} \frac{\sin\left(\tilde{k}(\tilde{r} - t|v_g|)\delta\theta\right)}{\tilde{r} - t|v_g|} e^{-\tilde{k}^2/4} \end{aligned} \quad (\text{S7})$$

where $\delta\theta$ is a small cut-off angle and $|v_g| = (\gamma\mu_0 M_0/\tilde{k})|\sin 2\varphi|\sqrt{H/(H + M_0 \cos^2 \varphi)}$. Eq. (S7) catches most features observed in Figs. 4(left) as summarized above: (i) $\cos\left(t \gamma \mu_0 \sqrt{H(H + M_0 \cos^2 \varphi)}\right)$ is an angle-dependent oscillations, i.e., reproduces the star-like feature. (ii) $\exp[-\alpha t \gamma \mu_0 \sqrt{H(H + M_0 \cos^2 \varphi)}]$ explains the angular dependent attenuation, revealing that rays with $\varphi \simeq \pi/2$ decay slower than those for $\varphi \simeq 0$. At large damping a radial pattern is visible near the y but not in the x -direction [see Fig. 4(b,left)]. (iii) The radial integral is a function of $\tilde{r} - t|v_g|$ only, therefore predicts that the wave packet expands with the group velocity $|v_g|$.

4. MAGNITUDE OF IFE

Here we estimate the magnitude of the IFE based on the experiments by Satoh *et al.* [9], who excited spin waves in a 110 μm thick $\text{Gd}_{4/3}\text{Yb}_{2/3}\text{BiFe}_5\text{O}_{12}$ film by laser light with pump fluence of $200 \text{ mJ}(\text{cm})^{-2}$ and pulse width of 120 fs at wavelength 1400 nm, and measured Faraday rotations of a linearly polarized probe pulse (at wavelength 792 nm) of the order of $\vartheta_{\text{F}} \sim 1 \text{ mrad}$. Satoh *et al.* do not measure the Verdet constant. In Bi-YIG (with unspecified doping concentration) the Verdet constants are $V \sim 5800, 1050, \text{ and } 380 \text{ rad m}^{-1}\text{T}^{-1}$ for wavelengths 543nm, 633nm, and 780nm, respectively [10]. The Verdet constant in $(\text{BiYbTb})_3\text{Fe}_5\text{O}_{12}$ at 780 nm was found to be $V \sim 8.5 \times 10^4 \text{ rad m}^{-1}\text{T}^{-1}$ [10]. Here we adopt $V = 10^4 \text{ rad m}^{-1}\text{T}^{-1}$ for both pump and probe fields.

The IFE and FE may be formulated in terms of a phenomenological free energy [11, 12]

$$F = \beta_{\text{pump}}(\mu_0 M_z) I_{\text{in}}, \quad (\text{S8})$$

where β_{pump} is a magneto-optical susceptibility at the pump laser frequency and I_{in} is the intensity of (right-hand) circularly polarized light. The effective field $H_{\text{IFE}} = -(1/\mu_0)\partial_{M_z} F = -\beta_{\text{pump}} I_{\text{in}}$. In the same theoretical framework, the Faraday rotation induced in the external field-free limit by $B = \mu_0 M_z$ reads

$$\vartheta_{\text{F}} = \frac{2\pi c_0}{\lambda_0} \beta_{\text{probe}}(\mu_0 M_z) L = V_{\text{probe}}(\mu_0 M_z) L, \quad (\text{S9})$$

where c_0 , λ_0 , and L are the velocity of light in vacuum, the wavelength of the probe pulse, and the film thickness, respectively. This relation allow us to express β in terms of V .

We can now estimate (assuming $V_{\text{pump}} \approx V_{\text{probe}}$) $|\mu_0 H_{\text{IFE}}| = \mu_0 V \lambda_0 I_{\text{in}} / (2\pi c_0) \sim 0.2 \text{ T}$ for the experimental pump intensity. H_{IFE} when applied as a pulse with width τ_l generates a magnetization $M_y = \gamma \tau_l \mu_0 H_{\text{IFE}} M_0$ and $m_0 = M_y / M_0 \sim 0.004$. Disregarding damping, the precession in the external field $H \hat{x}$ preserves this amplitude such that $M_z \approx M_y$. This leads to $\vartheta_{\text{F}} \approx V(\gamma \tau_l \mu_0^2 H_{\text{IFE}} M_0) L \sim 0.5 \text{ mrad}$, in reasonable agreement with the observations [9].

-
- [1] E. Schlömann, J. Appl. Phys. **31**, 1647 (1960).
 - [2] C. Kittel, Phys. Rev. **110**, 836 (1958).
 - [3] S. A. Manuilov, S. I. Khartsev, and A. M. Grishin, J. Appl. Phys. **106**, 123917 (2009).
 - [4] A. G. Gurevich and G. A. Melkov, *Magnetization Oscillations and Waves* (CRC Press, Boca Raton, 1996).
 - [5] A. A. Serga, A. V. Chumak, and B. Hillebrands, J. Phys. D: Appl. Phys. **43**, 264002 (2010).
 - [6] M. A. Gilleo and S. Geller, Phys. Rev. **110**, 73 (1958).
 - [7] M. F. Lewis and E. Patterson, J. Appl. Phys. **39**, 1932 (1968).
 - [8] G. G. Siu, C. M. Lee, and Y. Liu, Phys. Rev. B **64**, 094421 (2001).
 - [9] T. Satoh, Y. Terui, R. Moriya, B. A. Ivanov, K. Ando, E. Saitoh, T. Shimura, and K. Kuroda, Nat. Photonics **6**, 662 (2012).
 - [10] J. G. Bai, G.-Q. Lu, and T. Lin, Sensors and Actuators A: Physical **109**, 9 (2003).
 - [11] P. S. Pershan, J. P. van der Ziel, and L. D. Malmstrom, Phys. Rev. **143**, 574 (1966).
 - [12] A. Kirilyuk, A. V. Kimel, and T. Rasing, Rev. Mod. Phys. **82**, 2731 (2010).